Supporting Information

for

Operation of Calcium-Birnessite Water-Oxidation Anodes: Interactions of the Catalyst with Phosphate Buffer Anions.

Emanuel Ronge,[a] Jonas Ohms,[b] Vladimir Roddatis,[a] Travis Jones,[c] Frederic Sulzmann,[c] Axel Knop-Gericke,[c] Robert Schlögl,[c,d] Philipp Kurz,[*b] Christian Jooss[*,a,c] and Katarzyna Skorupska[*,d,e]

[a]Institut für Materialphysik, Georg-August-Universität Göttingen, Friedrich-Hund-Platz 1, 37077 Göttingen, Germany.

[b]Institut für Anorganische und Analytische Chemie and Freiburger Materialforschungszentrum (FMF), Albert-Ludwigs-Universität Freiburg, Albertstraße 21, 79104 Freiburg, Germany.

[c]International Center for Advanced Energy Studies, Georg-August-Universität Göttingen, Tammannstr. 4, 37077 Göttingen, Germany.

[d]Max-Planck-Institut für Chemische Energiekonversion, Stiftstraße 34-36, 45470 Mülheim an der Ruhr, Germany.

[e]Fritz-Haber-Institut der Max-Planck-Gesellschaft, Faradayweg 4-6, 14195 Berlin, Germany.

E-mail contacts: *skorupska@fhi-berlin.mpg.de*

cjooss@gwdg.de

philipp.kurz@ac.uni-freiburg.de

Table of Contents

1. Experimental details.

1.1 Materials. With the exception of the Ca-birnessite powder, all chemicals used in this study were purchased commercially and used as received. The electrolyte solutions were prepared using ultrapure water from an ELGA PURELAB flex 4 water-purification system (resistivity >18 MΩ·cm) and the following analytical grade chemicals (provider's name in brackets): KOH (Sigma Aldrich), KH_2PO_4 (VWR), K_2HPO_4 (Grüssing), imidazole (Chempur), H_2SO_4 (VWR) and K_2SO_4 (Roth).

The OER catalyst material used for this study was a previously described, synthetic Ca-birnessite of the approximate stoichiometry $Ca_{0,2}MnO_{2.21} \cdot 1.4H_2O$[1] which was screen-printed onto FTO-coated glass slides (Sigma Aldrich, 7 Ω·cm^{-2}) following a reported procedure.[2] As small modifications to the preparation steps described in ref.[2], the oxide suspension ("ink") was placed in an ultrasonic bath for 1 minute both at the beginning and the end of the 12 h stirring phase to ensure the homogeneous distribution of the oxide particles and to break down larger aggregates. This, together with an overall improvement of the entire "production sequence" and a slightly higher applied voltage (η = 490 mV here *vs.* 480 mV in ref.[2]). might explain why higher (factor ~2) and also more stable OER currents were observed in this work compared to the otherwise very similar electrolysis experiments reported by some of us already in 2014 for Ca-birnessite on FTO in neutral phosphate buffer. We generally found that small changes to the electrode preparation procedure can significantly influence the outcome of electrochemical measurements. Thus, we made sure that comparative experiments (as e.g. the ones shown in Fig. 1) were carried out using a single set of electrodes prepared as one batch starting from the same ink suspension, undergoing the same heat treatment side-by-side in the oven etc. Nevertheless, we are of course aware of the fact that complicated, multi-layer material systems like the electrodes used here will show some variability from piece to piece.
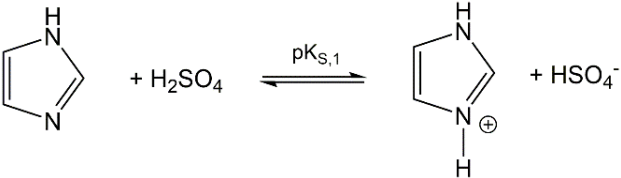
Important general remark: We have to admit that our logistically demanding co-operation between sample preparation (in Freiburg), electron microscopy measurements (in Göttingen) and X-ray spectroscopy (in Berlin) was not perfectly orchestrated at all times over the about two years it took for all experiments presented here to be carried out. As a result of minor miscommunications between some of us, the careful reader will find that there are e.g. experiments with phosphate buffer concentrations of 70 mM, others using 100 mM, we present CA traces and samples prepared at +1.71 V, another for +1.8 V or electrolysis times for sample preparations differing between 9 and 16 h. This is unfortunate and we are very disappointed that these mistakes have occured - however, we can hardly imagine that these inconsistencies could have a dramatic effect on the overall picture on phosphate / birnessite interactions obtained from our experiment and thus decided to present the dataset available to us at the moment as it is.

1.2 Electrocatalysis. Electrochemical experiments were carried out using a Princeton Applied Research Versastat 4 potentiostat / galvanostat equipped with a FRA module for electrochemical impedance spectroscopy (EIS) measurements. All experiments were carried out in standard 100 mL electrochemical cells (Metrohm) in a three-electrode configuration consisting of a double junction Ag/AgCl reference electrode (Metrohm, inner electrolyte 3 M KCl), a Pt rod counter electrode and the Ca-birnessite electrodes serving as working electrodes. An overview of the employed electrolyte solutions is given in Table S1. All cyclic voltammograms were iR-compensated to 100 %. Prior to the experiments, the uncompensated resistance was determined by EIS. Please note that all experimental electrode potentials given in this report have been converted to the reversible hydrogen electrode (RHE) scale:

$$E_{RHE} = E_{Ag/AgCl} + 0.207 + 0.059 \, pH \quad \text{(in V)}.$$

Thus, as an example, the potential applied during the chronoamperometry measurements shown in Fig. 1 in the main text (pH 7, +1.71 V *vs.* RHE) corresponds to $E_{Ag/AgCl}$ = +1.09 V applied to the working electrode by the potentiostat during the experiment in our setup.

Table S1. Compositions, basic properties and relevant buffering acid / base pairs of the three electrolyte systems used in this study. The total concentration of phosphate, imidazole or sulphate was 0.1 M in each case, respectively.

electrolyte	pH	κ / mS cm^{-1}	buffering acid / base pair
phosphate$^-$	7,0	15,7	$H_2PO_4^- + H_2O \xrightleftharpoons{pK_{s,2}} HPO_4^{2-} + H_3O^+$
borate	9.2	5.4	$HB_4O_7^- + H_2O \xrightleftharpoons{pK_{s,2}} B_4O_7^{2-} + H_3O^+$
methyl-phosphonate	7,0	10,5	
imidazolium sulphate	7,4	15,4	
potassium sulphate	7,0	20,3	-
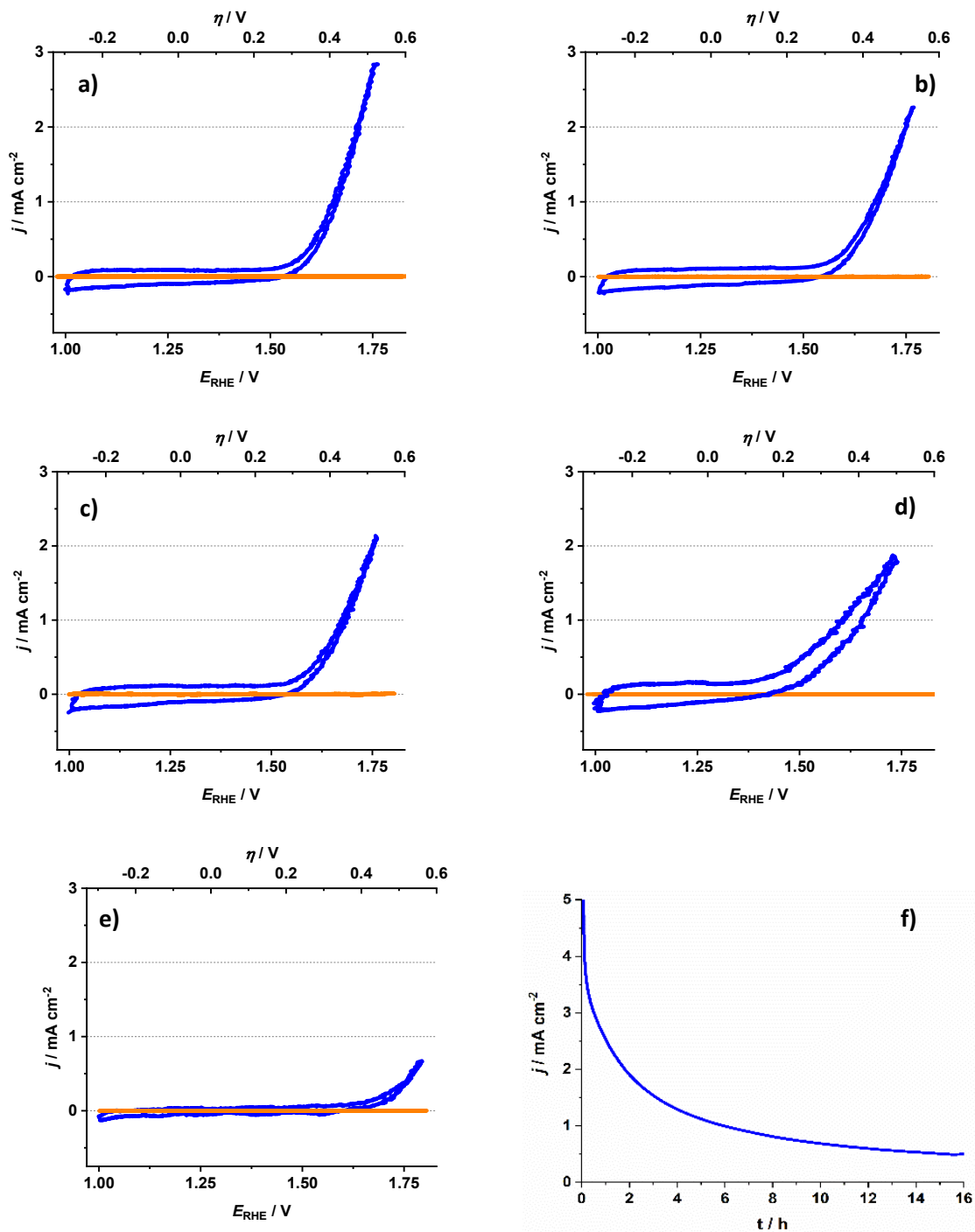
Figure S1. Cyclic voltammograms of Ca-birnessite-coated FTO-slides immersed in a) phosphate (pH 7), b) borate (pH 9.2), c) methylphosphonate (pH 7) and d) imidazolium (pH 7 and e) acetate (pH 4.8) buffer solutions. Fig. S1 e) shows voltammograms for a (non-buffering) potassium sulphate solution for comparison. In each case, the CV for the fifth cycle is shown. Orange curves indicate data for bare FTO-coated glass slides immersed in the respective electrolytes. The concentrations of the respective buffer anions were carefully adjusted to 0.1 M. The CV sweep rate was set to 20 mV·s^{-1} in all cases. f) Long-term chronoamperometry of a Ca-birnessite / FTO electrode at +1.8 V vs. RHE (η = 580 mV) in 0.1 M phosphate buffer (pH 7).

2. Electron Microscopy
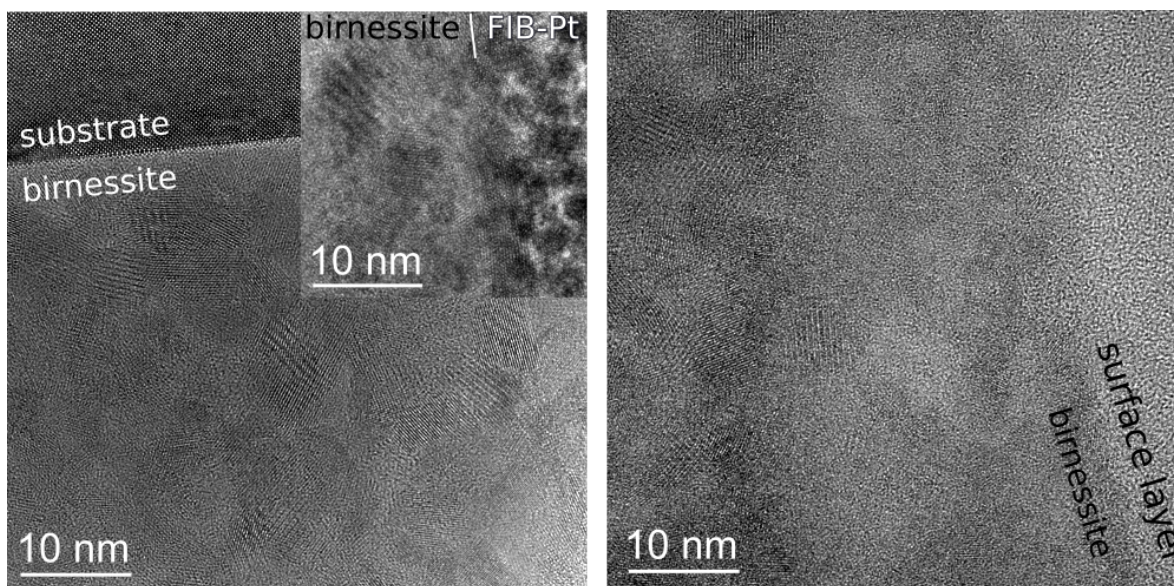
Figure S2. HRTEM-image of a Ca-birnessite electrode coated with a 0.2 µm thick catalyst layer. Left: pristine sample with inset showing the pristine nanocrystalline surface; right: sample after 12 h of electrolysis the phosphate buffer.

Figure S2 shows two HRTEM-images of the ≈ 0.2 µm thick virgin sample (left) and another sample after 12 hours electrolysis (right) in the phosphate buffer at an overpotential of 533 mV at pH 7. Nanocrystals with a diameter of a few nanometers can be observed in both samples and is not influenced by the choice of the substrate. The nanocrystalline structure is in good agreement with the electron diffraction patterns in Figure S3, showing diffraction rings which are broadened due to the nm scale grain size. After electrolysis, the formed P-rich surface layer is visible. This surface layer is much less ordered than the primary birnessite and most probably is amorphous. In accordance with the EDX and EELS analysis in Figure 4 and 5 the thickness of the P-rich surface layer can be determined to 15-20 nm for the 200 nm thick sample. From the EDX measurements in Figure S5 a surface layer thickness less than 2 nm can be estimated for the inner parts of the 4 µm thick sample. The difference in thickness might be explained by accessibility of the inner pores and/or the increased porosity and surface area of the thicker sample when compared to the 200 nm thick sample.

In Figure S3, the selected area electron diffraction (SAED) pattern of two types of ≈ 4 µm thick birnessite films on FTO substrates are shown. Figure S3 A shows the virgin sample and B another sample after 9 h electrolysis. Rings with diffraction spots are in both cases visible. The measured lattice plane spacing is noted in the diffraction pattern as well as in the radial intensity profiles of the diffraction pattern in figure S3 C and D. Note that the diffractions reflexes at 1.52 Å and 1.77 Å for the as prepared sample are only visible in the SAED patter and not in the radial intensity profiles due to their sparse appearance. No significant changes in the lattice spacings can be observed after the electrolysis within the accuracy limit of 2%. In Table S2, the measured lattice spacings are assigned to lattice planes of birnessite. The structure model from Lopano et al.[3] and the electron atomic scattering factors from Colliex et al.[4] was used to calculate the plane spacing d_{hkl} and the structure factor F. Note that only theoretical lattice spacings are given for those hkl with a large structure factor. In both HRTEM and SAED no (002) lattice plane is visible despite

of its relative high structure factor ($F^2 = 6 \cdot 10^7$) indicating a poor c-axis ordering. Consequently {001} lattice planes are not included in Table S2 and in addition less intense in-plane lattice planes like (200) with a $F^2 > 10^5$ are added.
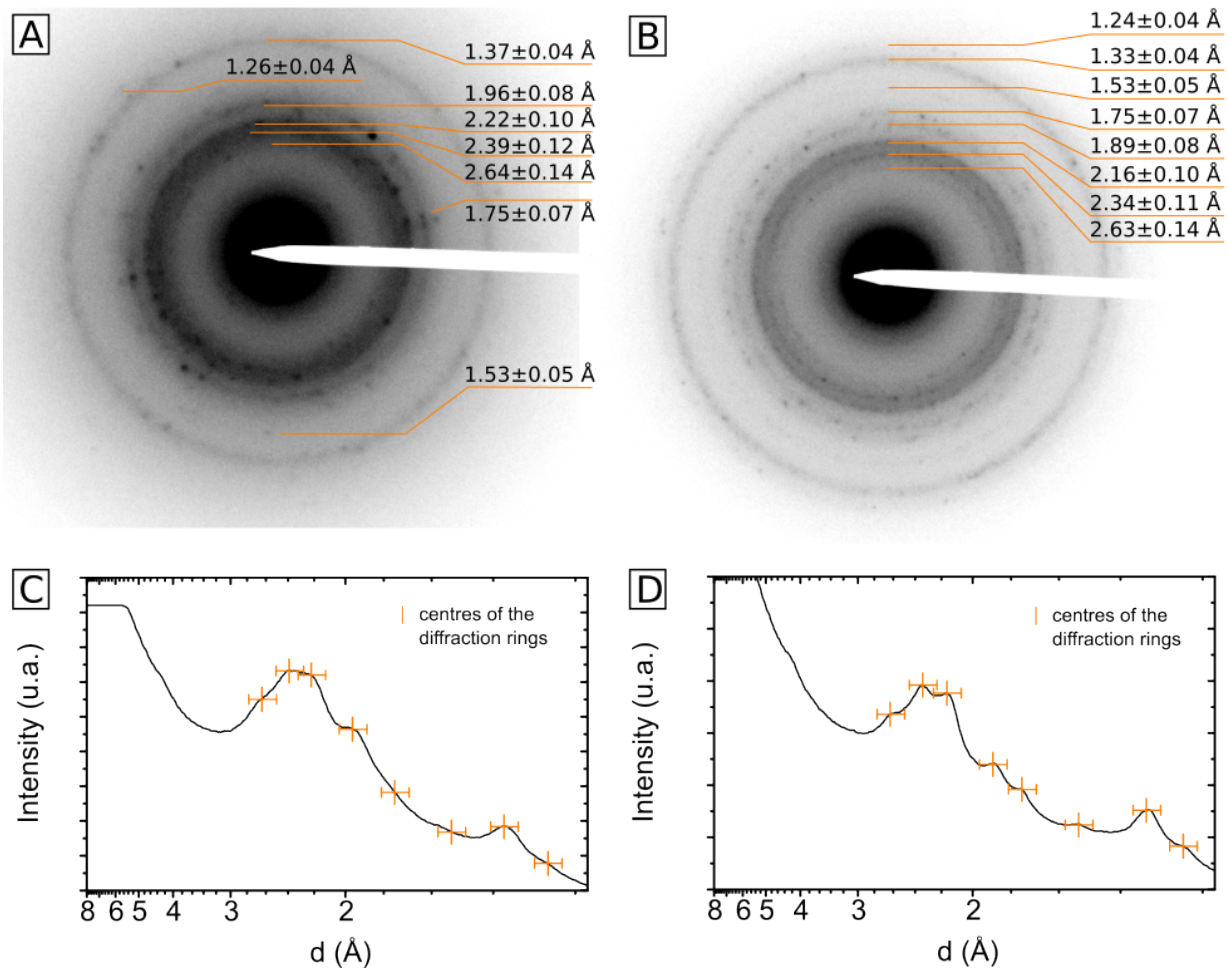
Figure S3. Electron diffraction pattern (top) and associated radial intensity profiles (bottom) of the Ca-birnessite layer. A and C: as prepared; B and D: after 9 h electrolysis in phosphate buffer.

The minor variation in intensity and broadness of the diffraction rings between the two samples are probably due to slight differences in the lamella thickness, grain size and number. Because of the relative breadth and partial overlap of diffraction rings, a distinct assignment of birnessite lattice planes to the diffraction rings is not possible. Instead Table S2 show which theoretical birnessite lattice planes are consistent with the diffraction rings within the measurement accuracy of 2% which is represented by the grey shading. Overall, the birnessite structure is in accordance with the diffraction data with three noticeable deviations: 1) The {001} lattice planes are missing probably due to a high c-axis disorder as mentioned earlier. 2) The (100) lattice plane at 5.05 Å overlaps with the zero beam and thus is not visible. 3) The diffraction ring at (1.53 ± 0.05) Å is very weak and broad. As a result, the calculated d_{hkl} reflexes in between 1.7 Å and 1.4 Å could be very well hidden in the flank, however, are not assigned to the data.

Table S2. Assignment of the lattice spacing to calculated lattice planes of birnessite. The calculated lattice planes which are within the 2% measurement accuracy of the experimental diffraction ring centres are indicated with a grey shading The structure model of Lopano et al.[3] and the atomic scattering factor from Colliex et al.[4] were used to calculate the structure factor F.

theoretical[3,4]			as prepared	after electrolysis
d Å	(hkl)	F^2	d Å	d Å
5.05	$\bar{1}00$	$1.02 \cdot 10^6$		
2.67	$10\bar{2}$	$2.46 \cdot 10^6$		
2.64	$0\bar{1}\bar{1}$	$1.56 \cdot 10^6$	2.64 ± 0.14	2.63 ± 0.14
2.53	$\bar{2}01$	$5.88 \cdot 10^6$		
2.52	$\bar{2}00$	$9.24 \cdot 10^5$		
2.49	110	$2.02 \cdot 10^7$		
2.47	$\bar{1}10$	$7.69 \cdot 10^6$		
2.42	$\bar{1}\bar{1}1$	$5.79 \cdot 10^7$	2.39 ± 0.12	2.34 ± 0.11
2.28	111	$3.27 \cdot 10^7$		
2.25	$\bar{2}0\bar{1}$	$2.72 \cdot 10^7$	2.22 ± 0.10	
2.12	$\bar{1}12$	$2.83 \cdot 10^7$		2.16 ± 0.10
1.95	112	$1.32 \cdot 10^7$	1.96 ± 0.08	
1.89	$\bar{2}\bar{1}0$	$9.46 \cdot 10^6$		1.89 ± 0.08
1.80	$\bar{1}\bar{1}3$	$9.78 \cdot 10^7$		
1.77	211	$1.11 \cdot 10^7$	1.75 ± 0.07	1.75 ± 0.07
1.68	$\bar{3}00$	$2.73 \cdot 10^6$		
1.64	113	$5.80 \cdot 10^7$		
1.58	212	$1.27 \cdot 10^7$		
1.58	$\bar{2}0\bar{3}$	$2.62 \cdot 10^7$		
1.51	$\bar{1}14$	$1.99 \cdot 10^7$	1.53 ± 0.05	1.53 ± 0.05
1.47	$\bar{3}\bar{1}1$	$1.37 \cdot 10^7$		
1.45	$\bar{3}10$	$9.63 \cdot 10^7$		
1.45	$\bar{3}\bar{1}0$	$2.70 \cdot 10^7$		
1.43	$\bar{3}\bar{1}2$	$3.06 \cdot 10^7$		
1.42	$\bar{3}12$	$8.31 \cdot 10^7$		
1.42	$0\bar{2}0$	$7.05 \cdot 10^6$		
1.40	$0\bar{2}\bar{1}$	$4.44 \cdot 10^7$		
1.39	213	$1.43 \cdot 10^7$		
1.38	$\bar{2}1\bar{3}$	$2.47 \cdot 10^7$		
1.37	$\bar{1}\bar{2}0$	$8.31 \cdot 10^6$	1.37 ± 0.04	
1.35	$\bar{2}05$	$3.20 \cdot 10^7$		
1.33	$\bar{3}13$	$1.43 \cdot 10^7$		1.33 ± 0.04
1.28	$\bar{1}\bar{1}5$	$6.67 \cdot 10^7$		
1.28	$\bar{4}01$	$3.52 \cdot 10^7$		
1.27	$\bar{3}1\bar{2}$	$4.76 \cdot 10^7$		

1.26	$12\bar{2}$	$1.11\cdot10^7$		
1.26	$\bar{4}00$	$1.19\cdot10^7$	1.26 ± 0.04	
1.24	$\bar{2}20$	$1.40\cdot10^7$		1.24 ± 0.04
1.24	$\bar{2}21$	$3.55\cdot10^7$		
1.24	$\bar{2}\bar{2}0$	$5.27\cdot10^7$		
1.22	$\bar{2}15$	$1.06\cdot10^7$		
1.22	$\bar{3}14$	$4.45\cdot10^7$		
1.21	$\bar{2}\bar{2}2$	$2.78\cdot10^7$		
1.21	$\bar{4}03$	$9.56\cdot10^7$		
1.21	214	$1.59\cdot10^7$		
1.20	$\bar{3}05$	$7.30\cdot10^7$		
1.20	$\bar{2}22$	$2.07\cdot10^7$		
1.20	$\bar{4}0\bar{1}$	$2.40\cdot10^7$		
1.19	115	$7.15\cdot10^7$		
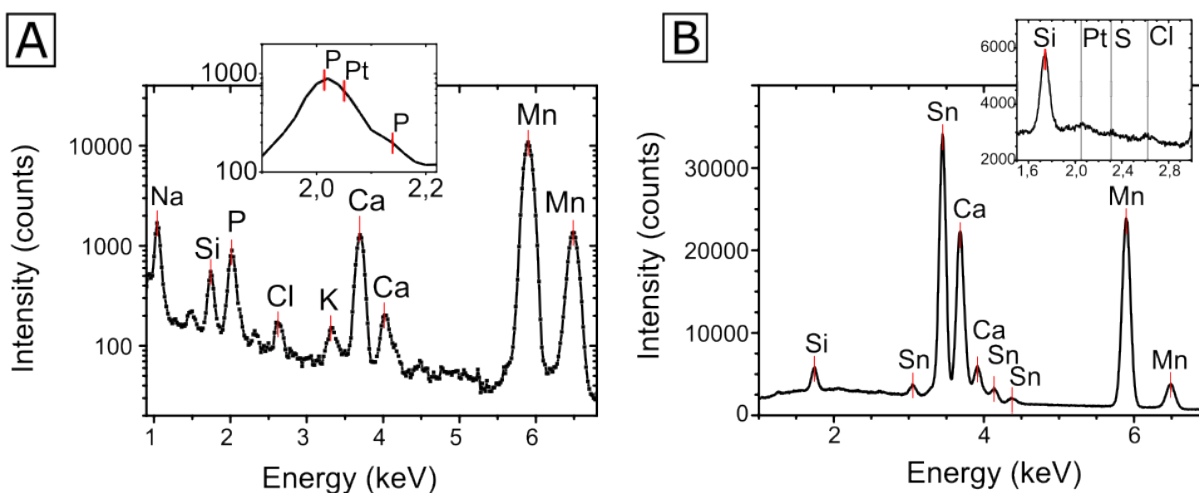
Figure S4. EDX element analysis of birnessite after electrolysis in different electrolytes. A: TEM EDX sum spectrum from the elemental mapping shown in Fig. 4A right in the main text (~4 μm thick birnessite electrode after 9 h of electrolysis in Na-phosphate buffer ($\eta = 530$ mV)); B: SEM EDX 4x4 point grid of 4 μm thick birnessite electrode after 9 h of electrolysis in H_2SO_4 adjusted with Imidazole to pH 7. The Si peak is a spurious signal from the detector and the small Sn signal originate from the substrate (FTO). The slight traces of Cl might stem from a tiny leak of the AgCl reference electrode

Figure S5 shows an EDX linescan of a 4 µm thick sample after 9 h of electrolysis. The red arrow in the HAADF-image points the direction and position of the scan. In comparison to the linescan in Figure 5 C of the main text, the spatial resolution is much higher. The Mn-concentration roughly correlates to the thickness contrast of the HAADF-image and shows to separate particles. The highest P/Mn-ration can be found at the edge of the pore. This is in agreement with the linescan shown in Figure 4 C. Within the particle the P/Mn-ratio is not significant, however, the P/Mn-ratio increases close to the interface between the two particles. To strengthen the significance of the P/Mn ratio, the EDX spectra for selected points are also shown in Figure S5. The EDX spectra clearly present a Phosphorous signal at the pore surface at spectrum #2, 7 and 8. Within the particle the P-signal is close to the noise level which is exemplified by spectra #3 and 6. The high P/Mn ration for the first measuring point appears only because of the Manganese content is close to zero. Since the P signal is close to the noise level in spectrum 1, we cannot determine an accurate P/Mn ratio and thus no error bar is plotted for the P/Mn ratio. This indicates that in addition to the electrode surface and the surfaces of the pores, phosphorous is also located on the surfaces / interfaces of the birnessite nanoparticles and is below a level of one atomic percent in the nanoparticles volume.
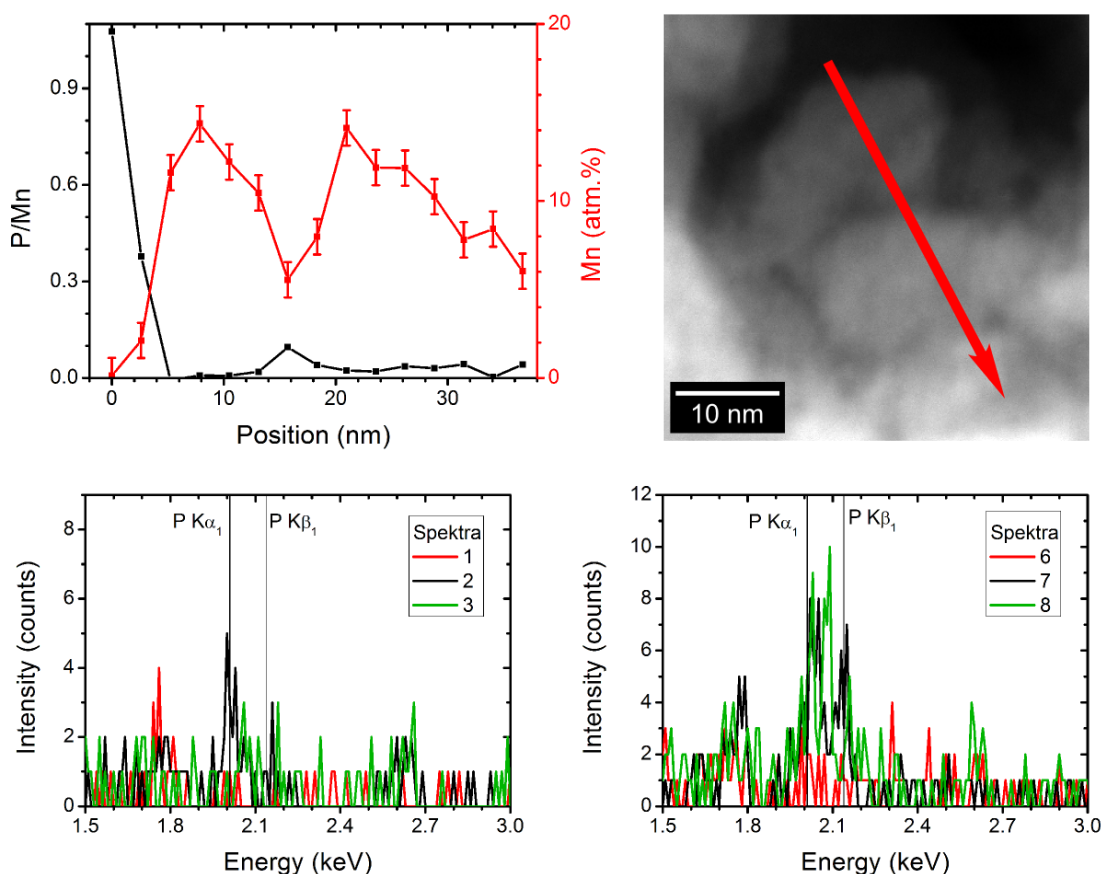

Figure S5. EDX linescan of a 4 µm thick sample after 9 h of electrolysis in phosphate buffered electrolyte. The spectra #1-3 and #6-8 correspond to the first 3 and the grain boundary data points in the top left figure.

3. Spectroscopy

Interestingly, a Mn^{2+} signal (peak at 640.5 eV) is also present in all samples except the powder sample. It is especially pronounced for freshly prepared electrodes, where Mn-reduction most likely occurs by the carbon-containing ink. Furthermore, studies shown that Mn^{2+} ions can also be generated by X-ray irradiation of MnO_x, so it cannot be ruled out that the described increase of the Mn^{2+} concentration is merely an artefact (however, concerning the issue of beam damage).[5]
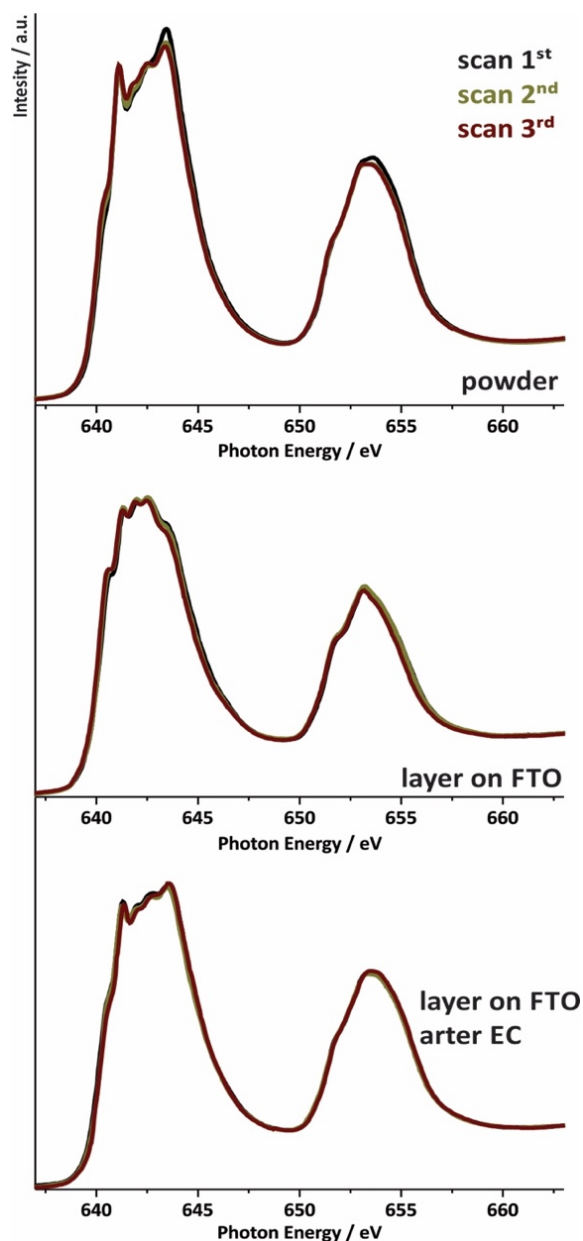
Figure S 6. Stability studies for NEXAFS Mn L-edge measurements. For each sample, a new spot was chosen and three full scans (625-670eV) were recorded on the same spot. *color code:* 1st spectrum – black, 2nd spectrum – dark yellow, 3rd spectrum – wine)
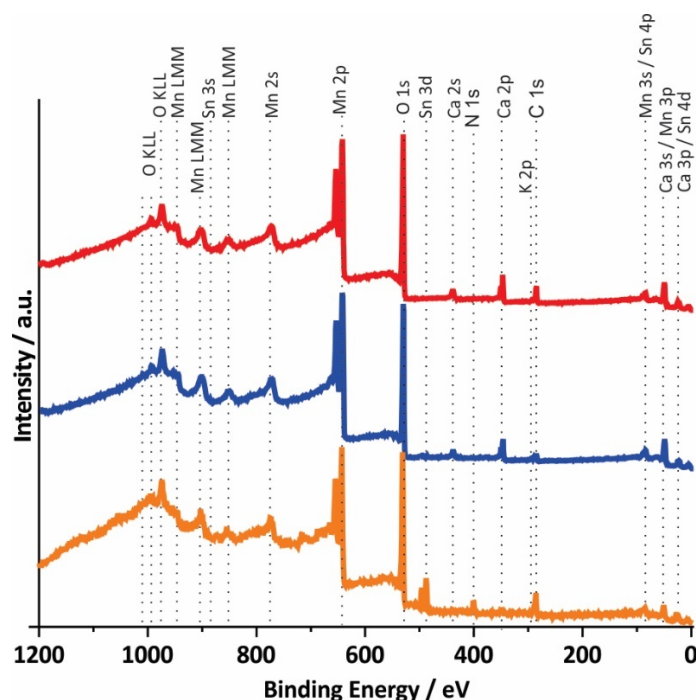
Figure S7. X-ray photoelectron survey spectra (XPS, hν = 1486.7 eV) of different Ca-birnessite samples. red: synthetic Ca-birnessite powder, blue: screen printed, 10 μm thick Ca-birnessite layer on FTO substrate after annealing at 450°C and orange: XPS of an electrode after 16 h of OER electrocatalysis in 0.1 M Imidazole – SO_4^{2-} buffer (η = 540 mV).
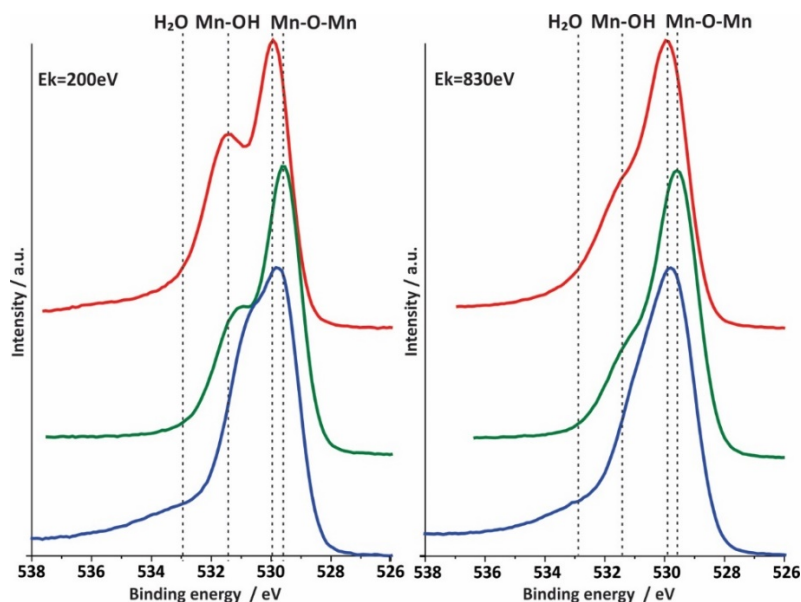
Figure S8. X-ray photoelectron spectra for the O 1s region for three Ca-birnessite samples: red: Ca-birnessite powder sample, green: screen printed, 10 μm thick Ca-birnessite layer on FTO substrate after annealing at 450°C and blue: XPS of an electrode after 16 h in 0.1 M phosphate buffer under OER conditions (η = 540 mV). The spectra on the left were recorded with a kinetic electron energy of 200 eV, those on the right for 830eV.

12

Reference spectra and linear combination analysis (LCA)

- **Reference spectra and difference spectra**
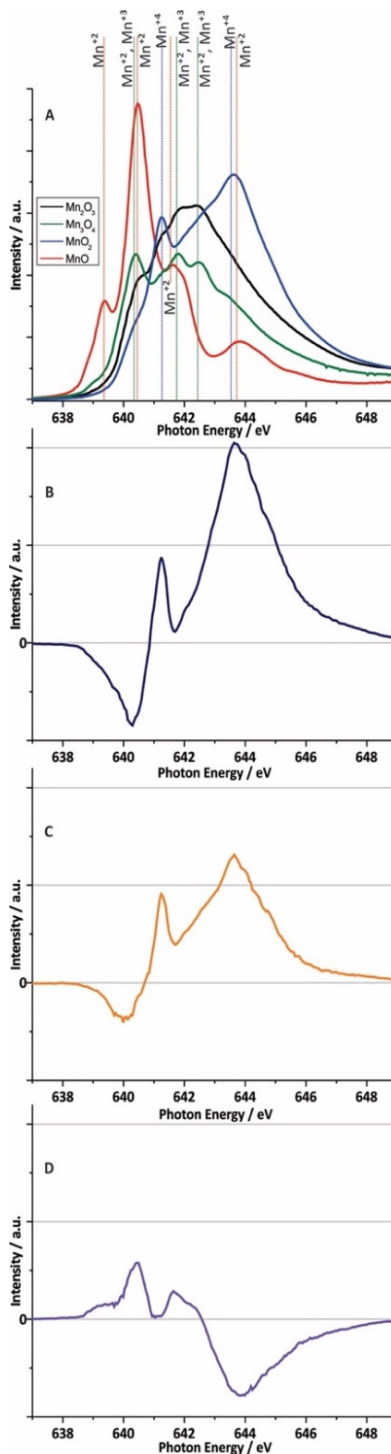
Figure S9. From the top: a) Mn L$_3$-edge reference spectra; c-d difference spectra of Mn L$_3$ edge; b) difference spectrum of the pristine electrode minus the powder Birnessite; c) difference spectrum of the pristine electrode minus the electrode after electrochemistry d) difference spectrum of the sample after electrochemistry minus the pristine electrode.

- **Linear Combination Analysis (LCA)**

Linear combination analysis (LCA) is performed by using a self-written python 3.7 script. MnO, Mn_3O_4, Mn_2O_3 and α-MnO_2 are used as components. A simple least square fit is applied to determine the composition of the of the investigated samples. A variety of 0.1 eV in excitation energy is allowed for the fitted data to account for uncertainty in energy calibration. Since the Mn L_3-edge is more sensitive to the local manganese environment, the fitted region is restricted between 638 and 648 eV excitation energy. Reference spectra and invested spectra are proceeded in the same way; photonflux normalization, linear background subtraction and normalization to the edge jump at 665 eV. The MnO, Mn_3O_4, Mn_2O_3 references (Fig. S9) were synthesized by the group of Philipp Kurz, University Freiburg. The MnO powder was heated to 200°C in UHV prior the reference spectrum was taken. The α-MnO2 reference powder was kindly provided by Justus Heese-Gärtlein (AG Behrens, Universität Duisburg Essen).[6]
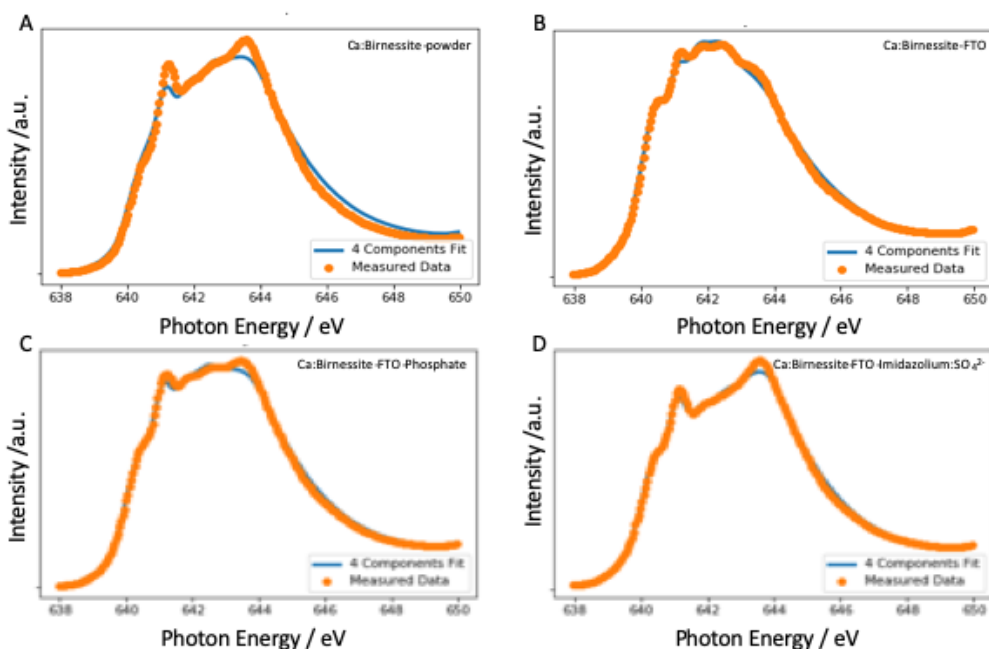
Figure S9a. The four component fitting results for studied samples: a) powder Ca:Birnessite; b) Ca:Birnessite-FTO pristine electrode; c) Ca:Birnessite-FTO-Phosphate the electrode after 16 h of OER electrocatalysis in 0.1 M phosphate buffer (η = 540 mV); d) Ca:Birnessite-FTO-Imidazolium:SO_4^{2-} electrode after 16 h of OER electrocatalysis in 0.1 M Imidazole – SO_4^{2-} buffer. Orange line – measured data, blue line – LCA fit.

Table S3a. Results of LCA for studied samples.

	MnO $Mn^{2+}_{(oct}$	Mn$_3$O$_4$ Mn^{2+}, Mn^{3+}	Mn$_2$O$_3$ Mn^{3+}	MnO$_2$ Mn^{4+}	Average oxidation state
Ca:Birnessite-powder	**0**	**0**	**41%**	**59%**	**3.59**
Ca:Birnessite-FTO-pristine	**7%**	**6%**	**65%**	**22%**	**2.99**
Ca:Birnessite-FTO-Phosphate	**2%**	**5%**	**45%**	**48%**	**3.56**
Ca:Birnessite-FTO-Imidazolium:SO$_4$$^{2-}$	**6%**	**7%**	**21%**	**66%**	**3.74**
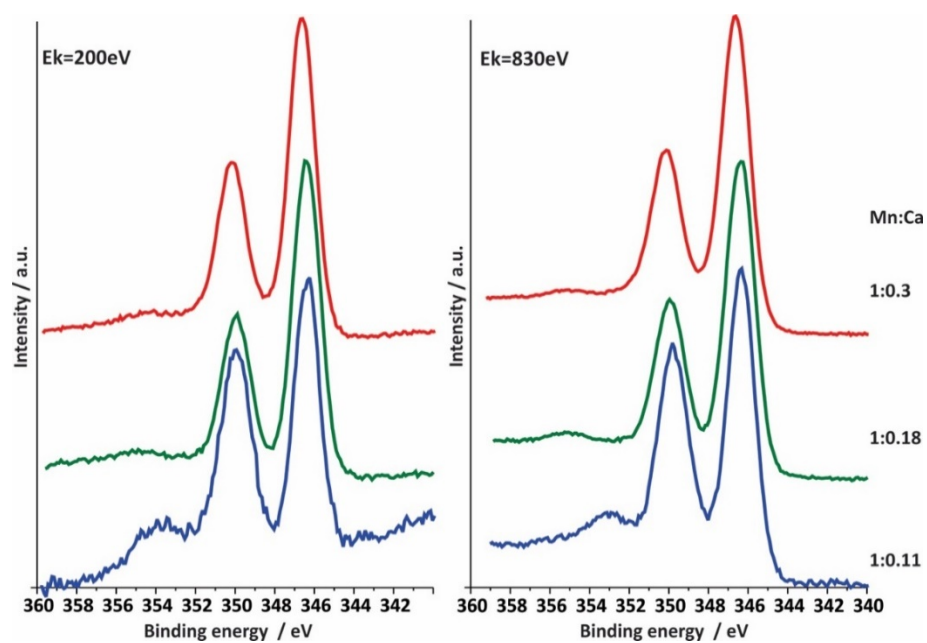
Figure S10. Ca 2p X-ray photoelectron spectra for three different Ca-Birnessite samples. The colour code is identical to the previous Figure S8 with the respective kinetic electron energies stated at the top.
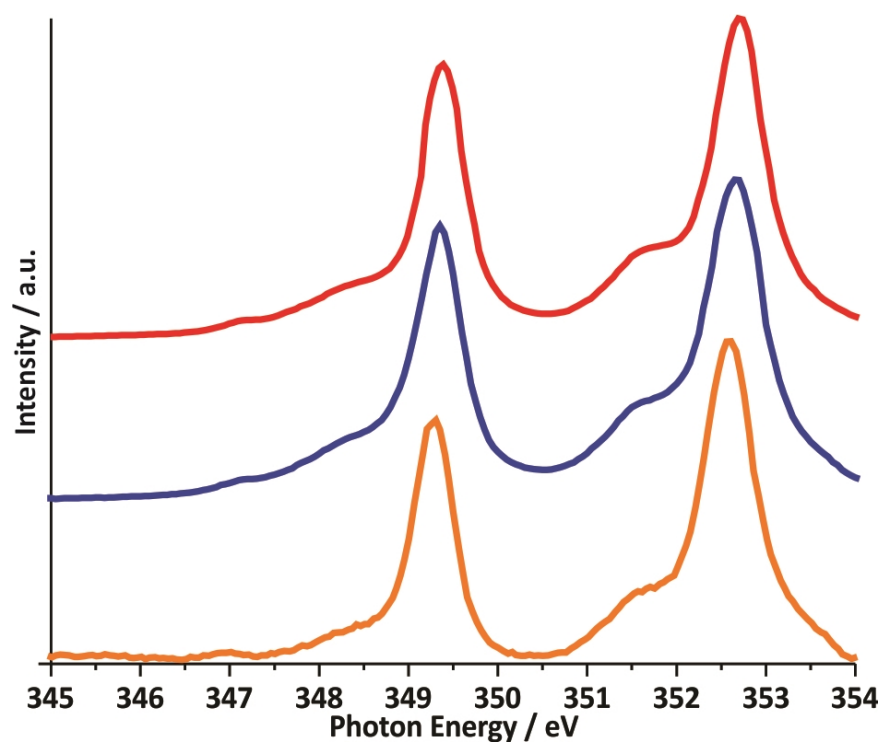
Figure S11. Ca L3-edge NEXAFS (TEY) spectra of the three different Ca-birnessite samples studied by XAS. Colour code and sample descriptions are identical to Figure S7.
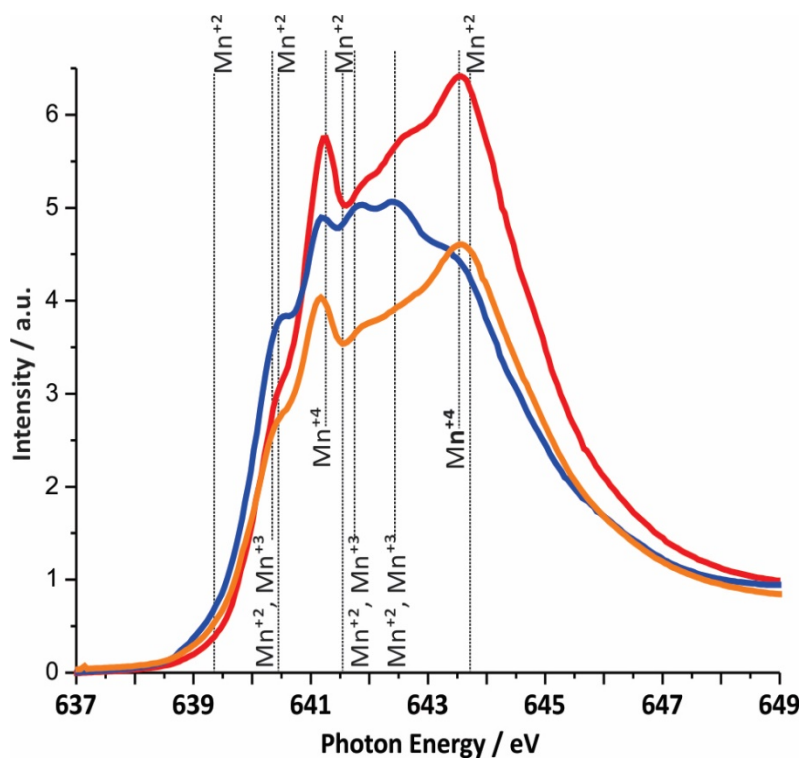
Figure S12. Mn L3-edge NEXAFS (TEY) spectra of the three different Ca-birnessite samples studied by XAS. Colour code and sample descriptions are identical to Figure S7.

Figure S13. Computed Ca L-egdes XA spectra and calculated Ca 2p XP spectra: To highlight the effects of the model parameters, (a) shows XAS calculations for a spherical Ca^{2+} ion along with two results for a Ca^{2+} io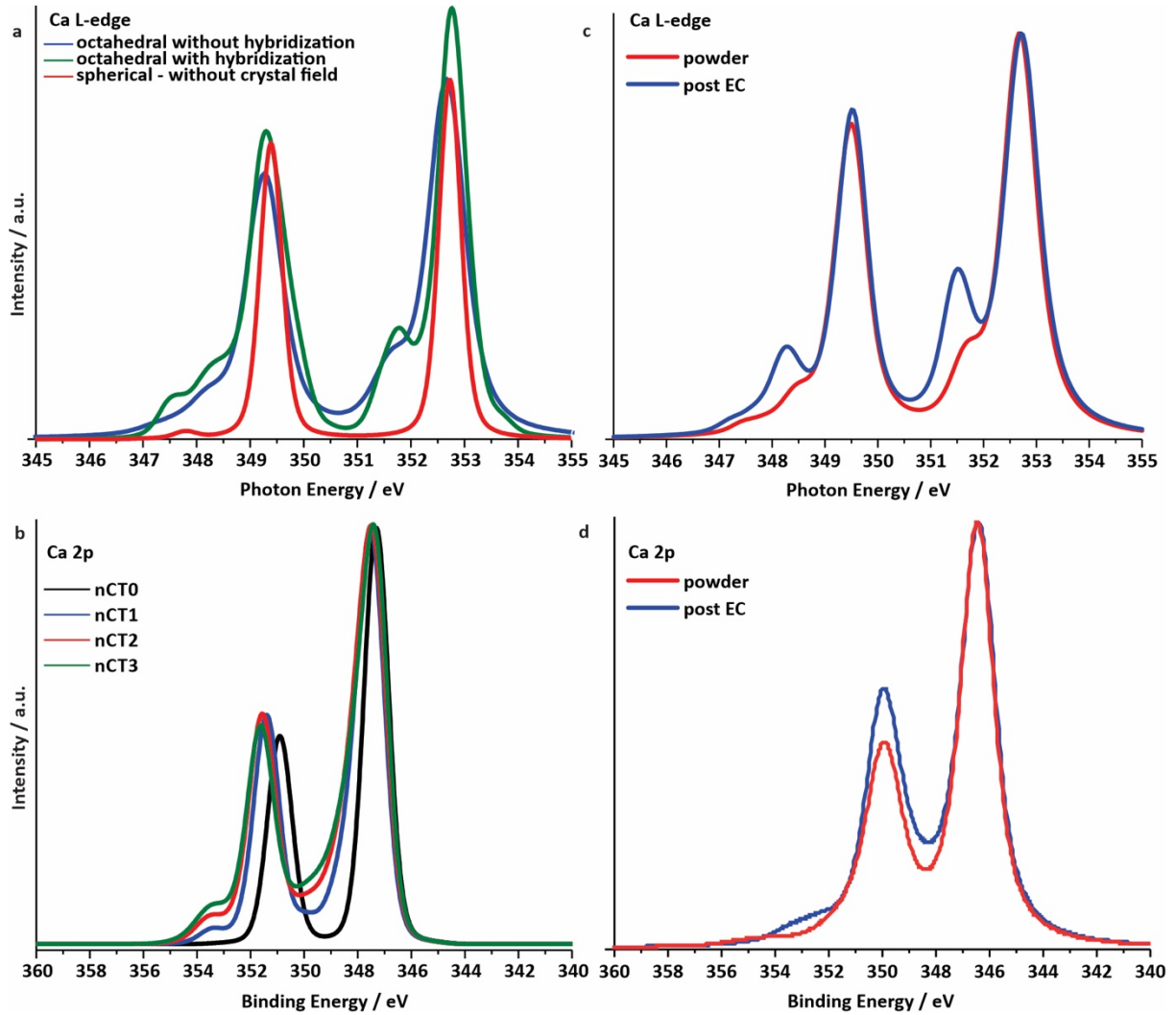n in an octahedral field with 10Dq=0.75 eV. The red line shows the result for spherical Ca^{2+} when hybridization between the Ca^{2+} ion and the ligand shell is ignored. The blue line shows the result for a Ca^{2+} ion in an octahedral field without hybridization. The green line shows the effect of including hybridization by allowing charge transfer from the ligand shell to the metal with a charge transfer parameter Δ=0.75 eV, i.e. a $|d^1\underline{L}\rangle$ configuration is included when describing the ground state. (b) The computed XPS spectra for a Ca^{2+} ion in an octahedral field with 10Dq=0.75 eV. The black line shows the result when there is no hybridization, which is simply the spin orbit split Ca 2p spectrum. The blue line shows the result when a $|d^1\underline{L}\rangle$ configuration is included, as with the XAS result. The ligand to metal charge transfer can be seen to give rise to a high binding energy satellite. The intensity of the satellite increases as higher $|d^n\underline{L}^n\rangle$ configurations are included, as shown by the red (green) line which includes configurations up to $|d^2\underline{L}^2\rangle \, (d^3\underline{L}^3\rangle)$, indicating the importance of charge transfer in describing the XP spectrum. (c) Shows the Ca XA spectra computed for the powder and post-EC material as computed with Quanty [Phys. Rev. B 85, 165113 (2012)] using 3 configurations. The spectrum of powder was recovered with V_{eg}=0.625 eV, V_{t2g}=0.45 eV, U_{dd}=3.5 eV, $U_{pd}=U_{dd}$/0.83, Δ=9 eV, and 10Dq=0.6 eV. The post-EC XA spectrum can be recovered by simply increasing 10Dq=1.0 eV; note the effect of hybridization on the XA spectra is weak. The powder parameters used to compute the XA spectrum also recover the XP spectrum (d)

of the powder. The post-EC XP spectrum, however is described by reducing Δ to 7 eV to increase the hybridization along with 10Dq=1.0 eV. The post-EC XA and XP spectra are then both described by the same model parameters.
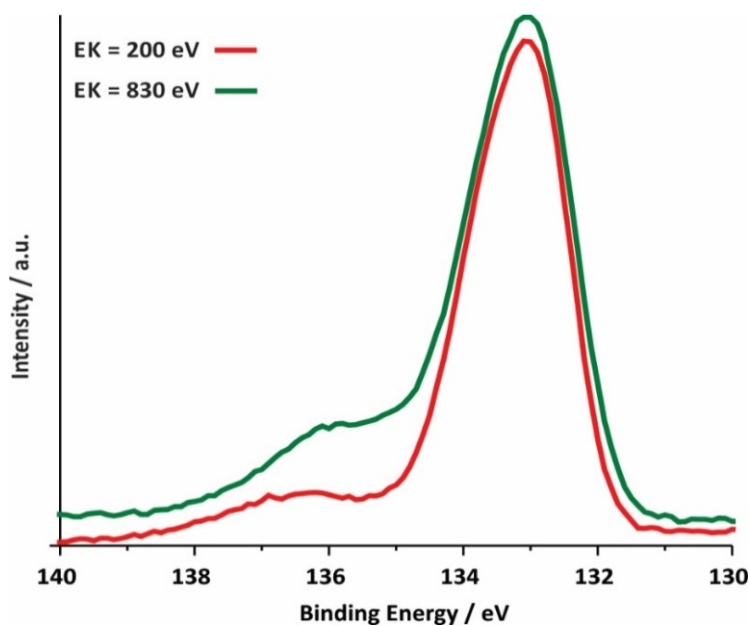
Figure S14. P 2p X-ray photoelectron spectra for Ca-birnessite electrode after electrolysis in phosphate buffer under OER conditions recorded at $h\nu$ = 960 and 330 eV (E_k = 830 (green) and 200 eV (red)).
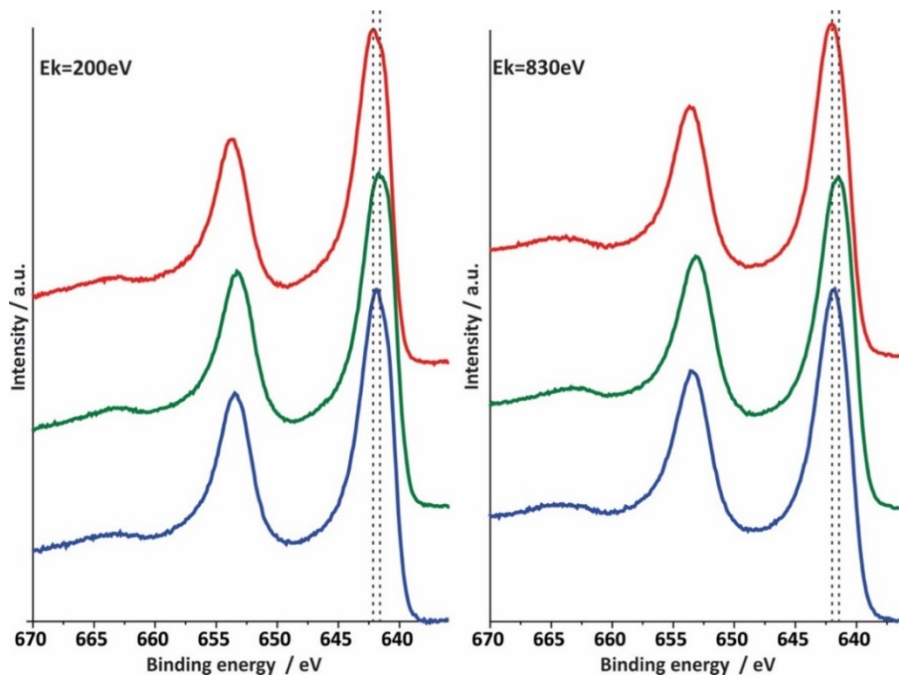
Figure S15. Mn 2p X-ray photoelectron spectra for three different Ca-Birnessite samples. The colour code is identical to the Figure S8 with the respective kinetic electron energies stated at the top. Due to significant multiplet splitting of the three oxidation states of manganese (II, III, IV), and the overlapping binding energy

for these multiplet splitting structures, the quantitative analysis of the Mn 2p spectra is not very reliable. For this reason, we based our analysis on NEXAFS Mn L-edges

Table S4. Comparison of the expected change in the Mn valence state due to charge neutrality with the measured change in Mn oxidation state determined by NEXAFS. The theoretical valence change is calculated based on the change in the Ca/Mn ratio determined by EDX.

	ΔCa/Mn	ΔMn Valence calc.	ΔMn Valence NEXAFS
Phosphate buffer	-0.1	0.2	0.2
Imidazolium sulphate	$\approx$-0.24	0.48	0.44

4. Theory: Hybridization and Calculation details.

Combining XAS and XPS give insight into the nature Ca before and after electrochemistry. XAS is sensitive to the crystal field, while hybridization between Ca and its ligand shell influences the charge transfer satellite(s) in XPS. In XAS the magnitude of the crystal field splitting can be seen to strongly influence the spectral shape, Figure S13a. In XPS, the distance between the main line and the satellite, denoting the degree of hybridization, depends both on the nature of the environment around Ca, which, in a octahedral field, can be parameterized by the ligand to metal hopping (V_{eg} and V_{t2g}) and charge transfer energy (Δ). If we consider only the monopole part of the Coulomb interactions, charge transfer will lower the energy of the final state in XPS by approximately Δ-U_{pd}, where Δ is the charge transfer energy and U_{pd} is the core-hole valence Coulomb interaction.[7] In this picture, we expect the Ca 2p XPS spectrum of birnessite to have a main peak for the $|cd^1L\rangle$ configuration and a satellite at higher binding energy due to the $|cd^0\rangle$ configuration, where $|c\rangle$ indicates the Ca 2p core hole. In other words, the first doublet of the spectra corresponds to a p^5d^1 final state, where the additional d-electron more effectively screens the core hole, and the higher binding energy doublet a p^5d^0 final state. To illustrate this point, we verified that hybridization can give the expected satellites by computing the XP spectrum within a charge-transfer multiplet model (ESI Figure S13b).[8] We began by computing the Ca 2p spectrum for a Ca^{2+} ion in spherical symmetry using a core line width of 0.17 eV before introducing crystal field splitting and hybridization. As expected, including crystal field splitting, does not lead to the appearance of a satellite. We then introduced hybridization, which led to the expected charge transfer satellite (see ESI, Figure S13 for details) and a ground state, $\Psi = \alpha|d^0\rangle + \beta|d^1L\rangle + \gamma|d^2L^2\rangle$..

With the applicability of our model ensured, we were able to interpret the measurements, beginning with the two spectra that show the charge transfer satellite (powder and after electrochemistry). Because U_{pd} should be nearly constant the observed differences would imply a change in covalency, which we modeled numerically for both the XA and XP spectra by way of multiplet ligand-field theory (MLFT) with the Quanty package.[9] As is typical, the model Hamiltonian was treated as a sum of three terms: an atomic term describing the central atom, a crystal field term, and a hybridization term. The first of these can be taken from a calculation on the isolated atom, where the Hartree-Fock values were scaled by 80%, while the latter can be fit to experiment to gain insight into the nature of the Ca-ligand interactions. From Figure S13a it is clear that unlike the XP spectrum, the XA spectrum is primarily sensitive to the crystal field term. Thus, we can use the XA spectrum to determine 10Dq of Ca in the pristine powder and after EC. Assuming Ca is octahedrally coordinated, we find Ca^{2+} in the powder with 10Dq~0.6 eV, while after electrochemistry 10Dq increases to 1.0 eV and Ca remains Ca^{2+}. Using these values we can then determine the hybridization from the Ca 2p XP spectra. We find the powder sample is characterized by weak hopping (V_{eg}=0.625 eV,

V_{t2g}=0.45 eV) and a large charge transfer energy (9 eV). The Ca^{2+} remaining after EC is characterized by a smaller charge transfer energy (7 eV) and larger crystal field splitting consistent with a change in the ligand shell that results in increased hybridization after EC. The small hopping in both cases, however, suggests Ca^{2+} remains intercalated rather than forming a phosphate or oxide phase, which would push the satellites to higher energies owing to an increase in orbital overlap in the phosphate/oxide phases.

5. References

1   C. E. Frey, M. Wiechen and P. Kurz, *Dalt. Trans.*, 2014, **43**, 4370–4379.

2   S. Y. Lee, D. González-Flores, J. Ohms, T. Trost, H. Dau, I. Zaharieva and P. Kurz, *ChemSusChem*, 2014, **7**, 3442–3451.

3   C. L. Lopano, P. J. Heaney, J. E. Post, J. Hanson and S. Komarneni, *Am. Mineral.*, 2007, **92**, 380–387.

4   C. Colliex, J. M. Cowley, S. L. Dudarev, M. Fink, J. Gjønnes, R. Hilderbrandt, A. Howie, D. F. Lynch, L. M. Peng, G. Ren, A. W. Ross, V. H. Smith, J. C. H. Spence, J. W. Steeds, J. Wang, M. J. Whelan and B. B. Zvyagin, in *International Tables for Crystallography*, International Union of Crystallography, Chester, England, 2006, pp. 259–429.

5   K. P. Lucht and J. L. Mendoza-Cortes, *J. Phys. Chem. C*, 2015, **119**, 22838–22846.

6   J. Heese-Gärtlein, Universität Duisburg-Essen , 2018.

7   A. E. Bocquet, T. Mizokawa, K. Morikawa, A. Fujimori, S. R. Barman, K. Maiti, D. D. Sarma, Y. Tokura and M. Onoda, *Phys. Rev. B*, 1996, **53**, 1161–1170.

8   J. M. Lopez Fernandez and O. A. Hernandez Rodriguez, *Teaching the Fundamental Theorem of Calculus: A Historical Reflection*, The MAA Mathematical Sciences Digital Library, 2012.

9   M. W. Haverkort, M. Zwierzycki and O. K. Andersen, *Phys. Rev. B - Condens. Matter Mater. Phys.*, 2012, **85**, 165113.